The Astrophysical Journal, 641:590–605, 2006 April 10

THE CALM BEFORE THE STORM: THE LINK BETWEEN QUIESCENT CAVITIES AND CORONAL MASS EJECTIONS

S. E. Gibson,[1] D. Foster,[2] J. Burkepile,[1] G. de Toma,[1] and A. Stanger[2]

Received 2005 September 13; accepted 2005 December 13

ABSTRACT

Determining the state of the corona prior to CMEs is crucial to understanding and ultimately predicting solar eruptions. A common and compelling feature of CMEs is their three-part morphology, as seen in white-light observations of a bright expanding loop, followed by a relatively dark cavity, and finally a bright core associated with an erupting prominence/filament. This morphology is an important constraint on CME models. It is also quite common for a three-part structure of loop, cavity, and prominence core to exist quiescently in the corona, and this is equivalently an important constraint on models of CME-precursor magnetic structure. These quiescent structures exist in the low corona, primarily below approximately 1.6 $R_\odot$, and so are currently observable in white light during solar eclipses, or else by the Mauna Loa Solar Observatory Mk4 coronameter. We present the first comprehensive, quantitative analysis of white-light quiescent cavities as observed by the Mk4 coronameter. We find that such cavities are ubiquitous, as they are the coronal limb counterparts to filament channels observed on the solar disk. We consider examples that range from extremely long-lived, longitudinally extended polar-crown-filament-related cavities to smaller cavities associated with filaments near or within active regions. The former are often visible for days and even weeks at a time and can be identified as long-lived cavities that survive for months. We quantify cavity morphology and intensity contrast properties and consider correlations between these properties. We find multiple cases in which quiescent cavities directly erupt into CMEs and consider how morphological and intensity contrast properties of these cases differ from the general population of cavities. Finally, we discuss the implications that these observations may have for the state of the corona just prior to a CME, and more generally for the nature of coronal MHD equilibria.

Subject headings: Sun: corona — Sun: coronal mass ejections (CMEs) — Sun: magnetic fields

Online material: mpeg animations

1. INTRODUCTION

Coronal mass ejections (CMEs), especially those originating near the solar limb, often exhibit a classic, "three-part" morphology of a bright expanding loop, followed by a dark cavity with a bright core embedded in it that can be identified as an erupting prominence (Illing & Hundhausen 1986; Fig. 1, *left*). An equivalent three-part structure of bright loop (or helmet streamer), cavity, and prominence core also often exists quiescently in the corona (Tandberg-Hanssen 1974; Fig. 1, *right*). Taken together, these quiescent and eruptive observations offer important clues to the nature of magnetic fields in the corona prior to and during CME eruptions. CMEs are thought to be driven by magnetic energy, stored in twisted or sheared magnetic fields. The exact nature of the pre-CME energized magnetic field is an important constraint on models of CME initiation. The common three-part morphology shared by quiescent precursor and erupting CME suggests a common magnetic structure that is in place prior to the eruption. We discuss this in more detail below.

Quiescent cavities can be observed at a range of wavelengths, but are most commonly seen in white-light observations. They typically exist in the low corona, below approximately 1.6 solar radii ($R_\odot$), at heights that are not currently observed by space-based white-light coronagraphs. At the present time they are visible in white light during solar eclipses or using the Mauna Loa Solar Observatory (MLSO) Mark IV (Mk4) coronameter. The Mk4 data are unique in allowing us to observe how white-light cavities evolve over the course of days, weeks, and even months, and are a rich resource for quiescent cavity observations. In this paper we use them in combination with other coronal data to achieve the first comprehensive study of quiescent cavities and their relation to CMEs. In § 2 we discuss observations and analyses of quiescent cavities to date. In § 3, we present the observed properties of the Mk4 white-light cavities we have analyzed, including their morphology and intensity contrast. In § 4 we present examples of cavities that erupt as CMEs and examine this subset relative to the wider data set for specific preeruptive characteristics. In § 5 we discuss the implications of our observations for coronal magnetic fields, and in § 6 we present our conclusions.

2. CAVITY OBSERVATIONS TO DATE

Quiescent cavities have been studied for decades (see Tandberg-Hanssen 1974, 1995; Engvold 1989 for reviews). The earliest analyses were of white-light eclipse data (Waldmeier 1941, p. 234; Waldmeier 1970; Saito & Hyder 1968; Saito & Tandberg-Hanssen 1973). The dense core sometimes seen within the cavity in white light is a prominence/filament, and early studies concluded that cavities were more likely to be visible when associated with quiescent filaments away from active regions and that their visibility was related to their size and the orientation of the filament axis relative to the line of sight (Waldmeier 1970). Early soft X-ray observations of the solar disk (Vaiana et al. 1973; McIntosh et al. 1976; Serio et al. 1978) demonstrated that the cavities overlie filaments, but more generally that they lie along neutral lines that may or may not contain filaments. This was borne out by EUV observations (Schmahl 1979) and helium 10830 Å observations (McCabe & Mickey 1981; Harvey & Gaizauskas 1998). Cavities are thus the limb counterpart to the filament channel on the disk,

[1] High Altitude Observatory, National Center for Atmospheric Research, P.O. Box 3000, Boulder, CO 80307-3000.

[2] c/o S. Gibson, High Altitude Observatory, National Center for Atmospheric Research, P.O. Box 3000, Boulder, CO 80307-3000.

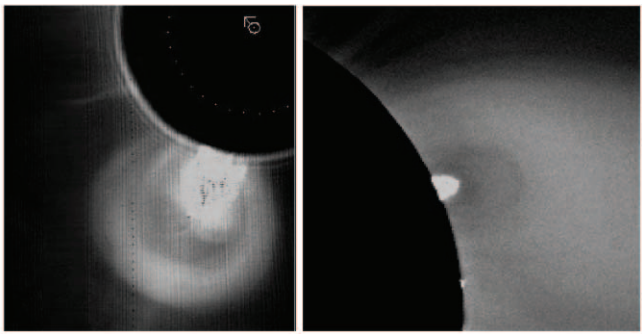

FIG. 1.—Three-part structures in white-light-containing cavities. Three-part CME in eruption (*left*) on 1980 August 18 (High Altitude Observatory/*Solar Maximum Mission* coronagraph). Quiescent prominence plus cavity (*right*) is seen in the 1988 March 18 Philippines eclipse image (National Center for Atmospheric Research/High Altitude Observatory Newkirk White-Light Coronal Camera [WLCC] telescope).

and can be seen in white light when they extend high enough and are favorably oriented to and reasonably unobstructed along the line of sight.

Early analyses of eclipse data made it clear that the cavities represented regions of reduced electron density (Waldmeier 1941, p. 234). A few quantitative estimates of this density depletion were made from these eclipse observations, with estimates of 80% or higher (Saito & Hyder 1968; Saito & Tandberg-Hanssen 1973). These estimates should be considered with great caution, however, as they use low-resolution eclipse photographs to estimate coronal brightness and from this determine coronal density, and they use highly simplified model assumptions of coronal morphology. Estimates were also made using radio observations of filament cavities and ranged from depletions of 20%–30% (Kundu et al. 1978) to 50% (Straka et al. 1975), to a recent estimate (Marqué 2004) of 25%–50%. Note that these radio estimates were relative to the "unperturbed" corona, as opposed to the white-light depletion estimates, which are relative to neighboring bright arches, and that they also make assumptions of coronal morphology and temperature. Early temperature estimates using EUV observations implied that cavities were at coronal temperatures (Schmahl 1979). More recent observations from the *Yohkoh* satellite have demonstrated interesting temperature structure occasionally visible within the cavity, for example, a hot sheath around the cold filament lying at its core (Hudson et al. 1999; Hudson & Schwenn 2000).

As coronagraph observations became available, it became possible to directly study the relationship of quiescent cavities to CMEs. Cases were found in which a quiescent cavity was observed to gradually rise, swell, and ultimately be released in a CME (Fisher & Poland 1981; Illing & Hundhausen 1985; Hundhausen 1999; Srivastava et al. 1999). More recently, Maricic et al. (2004) reported the eruption of a previously quiescent white-light cavity observed by the MLSO Mk4 coronameter, and a detailed kinematic study of this event was done using Mk4 and *Solar and Heliospheric Observatory* (*SOHO*) observations (Vrsnak et al. 2004). Two other such events were observed by *SOHO* EUV Imaging Telescope (EIT) and Large Angle and Spectrometric Coronagraph Experiment (LASCO) and were described in Yurchyshyn (2002) and Sterling & Moore (2004): although these eruptions occurred during Mk4 nighttime, the precursor cavities were observed by Mk4 on the days prior to the eruptions. We discuss the three CMEs described in Yurchyshyn (2002), Maricic et al. (2004), and Sterling & Moore (2004) further in § 4.

Direct low corona observations of the eruption of quiescent cavities have been few to date, however, because the transition from quiescent cavity into an erupting CME is not easy to capture observationally. The CME has to occur near enough in time to when a cavity is visible at the limb, and that visibility is very sensitive to cavity size, orientation, and obscuration by structures along the line of sight. Because cavities occur in the low corona, which has traditionally been observed in white light using ground-based coronameters, nighttime data gaps often interrupt observations. It is only the recent accumulation of high-quality, low coronal white-light observations that has allowed us to discover multiple cases of directly observed eruptions of quiescent cavities, which we present in § 4.

3. OBSERVATIONAL PROPERTIES OF Mk4 CAVITIES

3.1. *Unique Benefits of Mk4 Data Set*

Cavities observed in white light can be unambiguously identified as regions of lower density. EUV or X-ray off-limb observations do not require an occulting disk, and so have the advantage of imaging the cavity down to the solar limb. However, such emission observations often miss cavities visible in white light due to obscuration from nearby bright features, or else do not show the top of the cavity, so that its off-limb appearance is indistinguishable from a coronal hole. White-light cavity observations are also particularly useful for directly and quantitatively connecting these precursor structures to CMEs, generally also observed in white light.

The MLSO Mk4 coronameter provides unique low corona white-light observations. It has been in operation since 1998 November and is a significant improvement on the previous MLSO coronameter (Mk3) with regard to signal to noise, field of view, and spatial resolution. Mk4 also observes lower in the corona (down to 1.12 $R_{\odot}$) and has a longer observing day (up to 9 hr) than Mk3. At present, it is the only white-light coronameter regularly observing at heights low enough to include cavities. Data are freely available online in both fits and jpeg format.[3]

3.2. *Identification of White-Light Cavities for Analysis*

We define cavities as regions of coronal white-light intensity depletion, possessing two clearly distinguishable sides and a top. Our purpose here is not to attempt a truly systematic study, in the sense that we have not identified and analyzed every possible quantifiable cavity in the Mk4 observations. Indeed, Figure 2, which indicates three examples of cavities in our study with arrows, also shows several additional cavities not included in our study (examples include the cavities seen within the northwest streamer of the left-hand image and also within the southeast streamer of the middle image). Instead, we begin with a primary data set (set 1) that includes 88 days of cavity observations that relate to a seed set of 12 "best-case" cavities. These cavities were chosen because they were particularly clearly visible due to their size, intensity contrast, etc., when we surveyed all Mk4 observations from 1999 to 2004. A more systematic study would be worthwhile, as our best-case technique introduces a bias toward cavities associated with polar crown filaments (PCFs), which are filaments that are located at high latitudes and are usually longitudinally extended, so that line-of-sight obscuration is minimal. We have remedied this to some degree by also studying a secondary data set (set 2) of 10 days of quiescent cavity observations identified by working backward from seven clear three-part CMEs, which include smaller, less well defined, and often

[3] See http://mlso.hao.ucar.edu.

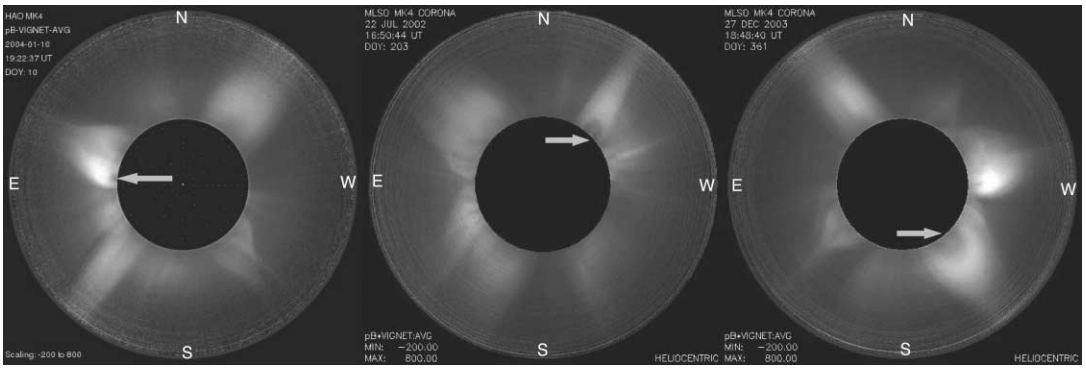

FIG. 2.—Examples of set 1 cavities observed in white light by MLSO Mk4 coronameter. 2004 January 10 (*left*), 2002 July 22 (*center*), and 2003 December 27 (*right*) (cavities 12, 8, and 11).

active-region-associated cavities. (Note that details of these observations are available online.)[4] Thus, our study is comprehensive if not systematic, and we leave the more complete survey as a future project.

3.2.1. *Identification of Set 1: "Best-Case" Cavities*

In our initial examination of the Mk4 data between 1999 and 2004, we chose 25 days as having the best observations of cavities. Table 1 lists these dates and cavity central polar angles. Figure 2 shows three examples, demonstrating the range of cavity sizes and central polar angles in our sample. However, doubtless because they were the most visible, all but one of these best-case cavities appeared at high latitudes in association with PCFs. Figure 3 shows a particularly nice example (cavity 8), where the PCF is oriented nearly parallel to the equator. PCFs are generally longitudinally extended, so that their associated cavities can be visible at the limb for several days in a row: in this case, for nine straight days. In another case (cavity 4) the underlying PCF channel was so extended that the cavity was sometimes visible on both limbs simultaneously. PCF-related cavities are also often long-lived, so that they are visible on and off for months, depending on the underlying filament channel orientation and obscuring features along the line of sight. Cases like these illustrate the intrinsic three dimensionality of cavities: they are the limb counterparts to filament channels, which when viewed in projection in the plane of the sky yield a daily cavity observation.

By studying the evolution of the cavities seen on these 25 best days, using Mk4 data as well as Hα and EUV observations of related filaments and filament channels, we were able to establish that only 12 independent cavities are actually represented, with some of our 25 best daily observations showing different views at different times of the same three-dimensional cavity. Table 1 indicates which of these 12 cavities each of our original 25 daily observations belongs to and also specifies one primary day (generally speaking, the "best of the best") for each cavity. In order to study the evolution of these cavities and to get a more comprehensive view of their range of visibility, we also analyzed adjacent days and reappearances at opposing solar limbs besides the original 25 days. This gives us our best-case data set, set 1, which includes a total of 88 days of observations related to the 12 cavities. Table 2 lists the dates of this expanded data set, grouped into the 12 best-case cavities. The nature of the filament/filament channel associated with each cavity is also listed, illustrating the strong bias toward PCFs introduced by choosing cavities based on visibility.

[4] See http://web.hao.ucar.edu/~sgibson/CAVITY/topcav.html.

3.2.2. *Identification of Set 2: Working Backward from CMEs*

Table 2 lists CMEs associated with the 12 set 1 cavities, demonstrating that most of these cavities erupted at least once in their lifetimes and in some cases were directly observed to do so by Mk4. In order to find more cases of quiescent cavities erupting

TABLE 1
ORIGINAL 25 BEST DAYS OF CAVITY OBSERVATIONS FOR SET 1

Dates	Polar Angle (deg)	Cavity	Primary Day
1998 November 3	24	1	Yes
1998 December 15	197	2	Yes
1998 December 16	197	2	No
1999 February 19	13	3	Yes
1999 October 1	150	4	No
1999 October 19	194	4	No
1999 November 2	146	4	No
1999 December 26	139	5	Yes
2000 March 15	205	4	No
2000 March 27	209	4	Yes
2000 March 30 (east limb)	205	4	No
2000 March 30 (west limb)	154	4	No
2000 April 13	202	4	No
2001 December 22	166	6	Yes
2001 December 29	330	7	Yes
2002 July 21	317	8	No
2002 July 22	317	8	Yes
2002 December 31	146	9	Yes
2003 January 6	220	9	No
2003 February 5	44	10	Yes
2003 February 6	219	9	No
2003 February 24	147	9	No
2003 October 25	136	11	No
2003 December 27	219	11	Yes
2004 January 10	85	12	Yes

NOTES.—"Best" days of cavity observations selected by surveying MLSO Mk4 white-light coronameter data from 1998 November to 2004 September. Many of these cavities are longitudinally extended, in some cases to the extent that they are visible at both limbs simultaneously (e.g., cavity 4). They can also be long lived, so that they are visible on and off for months, depending on underlying filament channel orientation and obscuring features along the line of sight. The 25 best days of observations represent views of 12 independent cavities. These 12 cavities are identified by number, and the primary day of observation for each is indicated (generally speaking, the day when a given cavity was observed most clearly). Polar angle (measured counterclockwise from north) shows the approximate location of the cavity center. Note that the Mk4 pointing is accurate to within $\pm 2^\circ$ from 2002 to 2004, but suffers a systematic error of up to 10° in earlier years.

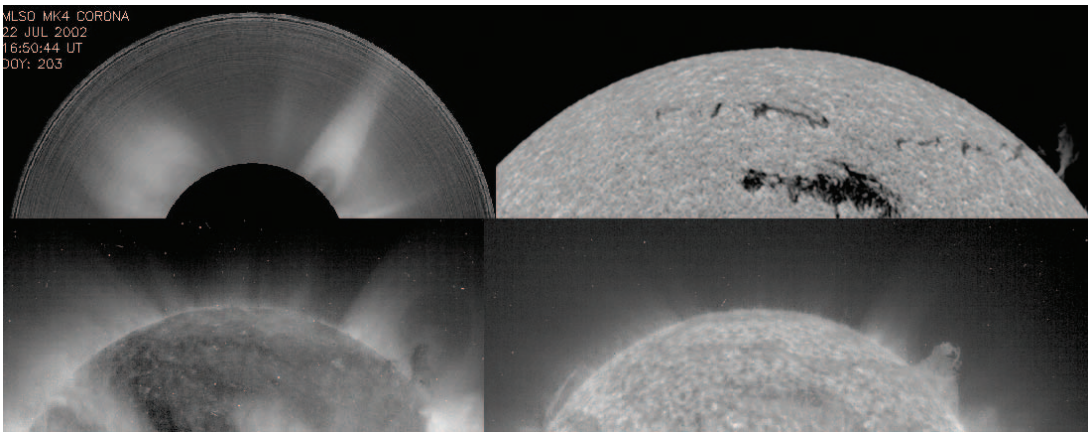

FIG. 3.—Observations of PCF-associated cavity (cavity 8) on 2002 July 21. *Top left*, white light (Mk4); *top right*, Hα (Big Bear Solar Observatory [BBSO]); *bottom left*, 284 Å (EIT); *bottom right*, 304 Å (EIT).

into CMEs and to move away from our PCF bias, we gathered a secondary database (set 2) of cavities by working backward from Mk4 three-part CMEs. This was accomplished by identifying such CMEs in MLSO event logs[5] and finding cases (other than those that could be associated with set 1 cavities) in which a quiescent cavity was observed prior to the eruption, either on the CME day or the day before. Table 3 lists four such cases in which both the CME and precursor cavity were observed by Mk4, along with three more cases in which Mk4 observed the quiescent cavity and, although the actual CME occurred during Mk4 night, the erupting cavity was observed by *SOHO* EIT. These include the two cases discussed in Sterling & Moore (2004), cavities 13 and 17 (cavity 17 was also discussed in Yurchyshyn 2002). Three additional neighboring days bring the total to 10 days analyzed for the seven cavities identified from CMEs: this is our set 2. These cavities are mostly still associated with fairly large filaments (the exception is cavity 19, which is associated with a small active region filament). However, unlike set 1, they lie at lower latitudes and often are in close proximity to active regions.

[5] See http://mlso.hao.ucar.edu/cgi-bin/mlso_logs.cgi.

3.3. *Analysis*

Now that we have identified our cavities, we need to quantitatively determine their morphological and intensity properties. Figure 4 demonstrates our analysis technique. On the left is a quadrant from a Mk4 observed image, showing white-light intensity, or polarized brightness (*pB*). On the right is a scan at 1.2 $R_\odot$ showing *pB* as a function of polar angle. We have developed an interactive code, in which the user identifies the top of the cavity and the approximate location of the cavity edges for a given day's observation. A more accurate location for the edges is then determined by the code at two heights (i.e., 1.2 $R_\odot$ and a height halfway between 1.2 $R_\odot$ and the top of the cavity) by finding the locations of the sharpest slopes (inflection points) in the intensity versus position angle line plot (see Fig. 4, *right side, vertical dashed lines*). The minimum intensity pixel within the cavity is then determined (*horizontal blue dashed lines*), as is the maximum intensity at the two bright rims of the cavity (*red and green horizontal dashed lines*).

From this information we can determine a range of morphological and intensity contrast properties. The width of the cavity is determined to be the distance between the two cavity edges (locations of sharpest slope). The center of the cavity is determined

TABLE 2
SET 1 CAVITIES

Cavity	Filament type	Days Analyzed	Associated CMEs
1.....	Curved PCF-N	2: 1998 Nov 2–3*	LASCO/EIT: 1998 Nov 11
2.....	PCF-S	8: 1998 Dec 12–(15*)–17; 1999 Feb 4–5	Mk4: 1998 Dec 19, 1999 Feb 5
3.....	PCF-N	2: 1999 Feb 18–19*	None detected (missing *SOHO*/MLSO data)
4.....	PCF-S	18: 1999 Sep 18–19; 1999 Oct 1,9; 1999 Nov 2,18; 1999 Dec 13; 2000 Feb 3–5; 2000 Mar 2–3,15,27*,30(b.l.); 2000 Apr 13(b.l.)	Mk4: 1999 Nov 19; 2000 Feb 5; 2000 Mar 3
5.....	Angled CF-S	2: 1999 Dec 26*,28	LASCO/EIT: 1999 Dec 29
6.....	PCF-S	3: 2001 Dec 19,20,22*	EIT filament eruption: 2001 Dec 23
7.....	Curved PCF-N	2: 2001 Dec 29*–30	None detected (possible back side LASCO: 2002 Jan 1)
8.....	PCF-N	24: 2002 May 16,18,27,29,31; 2002 Jun 12–13,25–27; 2002 Jul 8–10(b.l.),11,13; 2002 Jul 14–16,20–22*	LASCO/EIT: 2002 Jul 23
9.....	PCF-S	10: 2002 Dec 31*; 2003 Jan 6,9; 2003 Feb 6–8,10–11,23–24	EIT filament eruption: 2003 Jan 1
10.....	CF-N	1: 2003 Feb 5*	EIT filament eruption: 2003 Feb 7
11.....	PCF-S	15: 2003 Sep 25,27; 2003 Oct 9–10,21–22,24–26; 2003 Dec 12,14,21,24,26–27*	None detected (missing *SOHO*/MLSO data)
12.....	Circular filament	3: 2004 Jan 8–10*	LASCO/EIT: 2004 Jan 21

NOTES.—In two cases, although the filament was high latitude and longitudinally extended, there was a neutral line closer to the pole, so we have described them as crown filaments (CF) rather than polar crown filaments (PCFs). The primary cavity date for each is indicated with an asterisk. Cavities viewed at both limbs indicated by "b.l."

TABLE 3
SET 2 CAVITIES

Cavity	Polar Angle (deg)	Filament Type	Days Analyzed	Associated CMEs
13.....	40	Near AR 8889	1: 2000 Feb 26*	LASCO/EIT: 2000 Feb 26
14.....	56	Near AR 9461	1: 2001 May 15*	Mk4: 2001 May 15
15.....	107	Large angle to LOS	2: 2001 May 24,25*	Mk4: 2001 May 25
16.....	122	Large angle to LOS	3: 2001 Aug 8,9*	Mk4: 2001 Aug 9
17.....	59	Near AR 9773	1: 2002 Jan 3*	LASCO/EIT: 2002 Jan 4
18.....	306	Ending in AR 10223	1: 2002 Dec 27*	LASCO/EIT: 2001 Dec 28
19.....	293	AR filament (AR 10278/10287)	1: 2003 Feb 15,16*	Mk4: 2003 Feb 16

NOTES.—Primary day for each cavity is indicated with an asterisk. Associated filaments clearly not oriented favorably to the line of sight (LOS) are indicated. Polar angle (measured degrees counterclockwise from north) shows the approximate location of the cavity center. Note that the Mk4 pointing is accurate to within $\pm 2^\circ$ from 2002 to 2004, but suffers a systematic error of up to 10° in earlier years.

to be halfway between these edges. The depletion of pB in the cavity is determined with regard to both the poleward and equatorward bright rims by taking the ratio of the cavity minimum intensity to each rim maximum intensity (specifically, $1.0 - pB_{\rm cav}/pB_{\rm rim}$). The cavity sharpness is calculated also at both the poleward and the equatorward edges, as the slopes of pB versus polar angle at the locations of the cavity edges. It is in units of central solar brightness ($B_\odot$) per degree polar angle.

The error bars indicated in the plots and tables in this paper are estimated in the following manner. The absolute calibrated noise level of Mk4 pB is known to within 6×10^{-9} $pB/B_\odot$ (Elmore et al. 2003), and we have also included an empirically derived error of 1% pB as an additive uncertainty due to sky noise in the daily averaged images. To address systematic errors, the interactive analysis is performed three times for each cavity, so that the final error bars reflect the combined errors of the three runs. This systematic error generally reflects the noisiness of the data: we perform a smoothing over 3 pixels (1.°5), and because our original estimate of cavity edges determines the starting point of this running average smoothing function, a small change in the original estimate of the cavity edges can significantly affect results for noisy data. See Figure 5 for an illustration of this; note that the data are plotted here and in Figure 4 every 0.°5, with the line plot indicating the data smoothed over 1.°5. The top of the cavity is identified by the user by bracketing it interactively on the quadrant image, thus providing an error bar on the height of the cavity, which is compounded in a systematic manner over the three runs. The error for the positioning of the cavity edges, which affects width and sharpness errors, consists of the 0.°5 instrument resolution along with the generally more significant systematic component and is indicated by the distance between the pairs of vertical dashed lines at each edge. The errors for depletion arise from the systematic error in locating the minimum pB and maximum rim pB values, as well as from the range of the unsmoothed pB about the specified location, and are indicated by the pairs of parallel green, red, and blue horizontal dashed lines.

3.3.1. *Morphology*

In this manner we have analyzed cavity observations on the 88 days associated with set 1, as well as on the 10 days associated with set 2. The entire data set thus consists of 98 days of observations, representing 19 independent cavities. Table 4 shows the

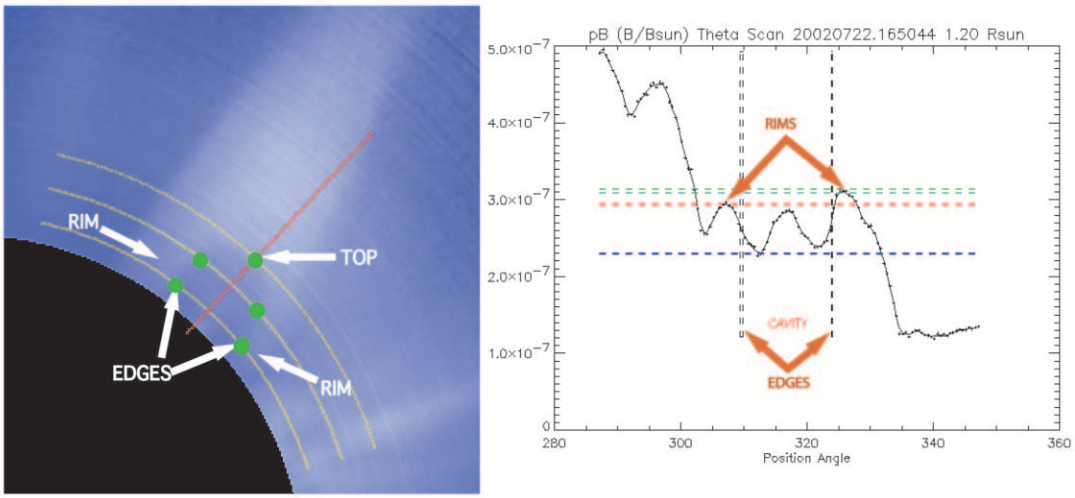

FIG. 4.—Example of analysis of cavity for 2002 July 22. *Left:* Quadrant close-up of cavity as observed in white light by the Mk4 coronagraph. Yellow arched lines are positioned at three heights, at the top of the cavity, 1.2 $R_\odot$, and halfway in between. The center of the cavity is indicated by the red radial line, and the edges by the green circles. *Right:* Latitudinal scan of polarized brightness (pB) in units of central solar brightness ($B_\odot$) at a height of 1.2 $R_\odot$, corresponding to the lowest yellow arched line in the quadrant image. Edges of the cavity corresponding to green circles in the quadrant image are indicated here by vertical dashed lines, with uncertainty indicated by double vertical lines. Minimum pB within the cavity is indicated by the horizontal blue line, and maximum pB at the poleward and equatorward bright rims are indicated by the green and red horizontal lines, respectively (these rims are also indicated on the left-hand quadrant close-up image). The intensity bump in the middle of the cavity is due to the presence of the central prominence.

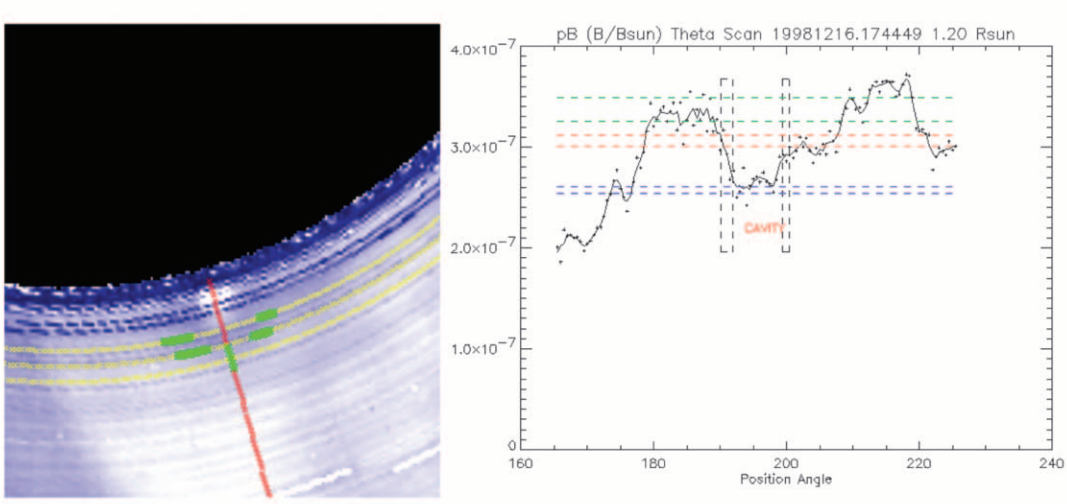

FIG. 5.—Example of analysis of a noisier cavity for 1998 December 16. *Left:* Quadrant close-up of cavity as observed in white light by the Mk4 coronagraph, as in Fig. 4. *Right:* Latitudinal scan of polarized brightness (*pB*) in units of $B_{\odot}$ at a height of 1.2 $R_{\odot}$, as in Fig. 4.

minimum, mean, and maximum values of cavity width (at 1.2 $R_{\odot}$), height, and distance of central polar angle from the equator. In order to compare independent observations, the first three rows are determined using only the primary days of observations for each cavity. The final row contains information from all 98 days analyzed.

Figure 6 plots morphological properties versus time for the 19 primary days of observations. From this and from the table it is clear that cavities in set 1 tend to be wider and centered at higher latitudes than those in set 2. This arises due to the selection bias toward PCFs prevalent in set 1 (see Table 2), as opposed to the association with filaments near or within active regions of many of the cavities in set 2 (see Table 3). Figure 6 demonstrates that the set 2 cavities also tend to have smaller heights. An exception is set 2 cavity 16: however, this cavity, along with the other set 2 case that did not have active region (AR) association (cavity 15), is associated with a filament oriented at a large angle to the line of sight. It is clear then why these set 2 cases did not make it into set 1; either their height, orientation, or proximity to bright line-of-sight features (as exist above active regions) made them relatively less visible. However, note that the bottom right plot in Figure 6 demonstrates a largely constant aspect ratio of cavity width (at 1.2 $R_{\odot}$) to height of 0.62 ± 0.08. If we make this calculation using only set 1 data, the aspect ratio is 0.55 ± 0.1, and if calculated using only set 2 data, it is 0.75 ± 0.16. Thus, the aspect ratio is consistent within error bars for both data sets.

3.3.2. *Contrast*

Tables 5 and 6 present quantitative information regarding how the cavity contrasts with the surrounding corona (note that there are fewer cavities analyzed here than in Table 4, because some cavities were too noisy to get meaningful intensity contrast information, although they could be analyzed for morphological features). In particular, we calculate cavity depletion by taking the ratio between the darkest portion of the cavity and the bright cavity rim for a given height (see Fig. 4). We also quantify cavity sharpness. The cavity edges have been defined as the inflection points in the white-light intensity versus polar angle plot, so we quantify the edge sharpness by determining the value of this maximum slope. We discuss the implications of a well-defined cavity boundary for the nature of the cavity magnetic fields further in § 5.

As discussed in § 2, historical estimates of cavity depletion have ranged widely and in some cases have depended on temperature assumptions. Because the observations presented here are white light, they are insensitive to temperature effects and can be directly related to electron density scattered along the line of sight (Billings 1966). However, white-light observations are sensitive to structures along the line of sight, which can affect contrast estimates in two ways. First, a bright structure in front of (or behind) a cavity will artificially increase the intensity within the cavity, thus leading to underestimates of depletion or sharpness. This is true both for intervening bright structures that are unrelated to the cavity (e.g., neighboring bright active regions) and for the cavity's own bright rim projecting onto its depleted region if the cavity orientation is not along the line of sight. Second, unrelated intervening bright structures could also affect contrast estimates by intersecting the rim of the cavity and increasing the apparent brightness of that rim, leading to an overestimate of cavity depletion and sharpness relative to that rim. For this reason we have separated our calculations into poleward and equatorward categories. Generally speaking, and for the primary days presented in Tables 5 and 6, the poleward depletion calculation is preferred, because the poleward rim is less likely than the equatorward rim to be affected by intervening bright features unrelated to the cavity.

Since intervening bright features may still increase the brightness of the cavity itself, the minimum cavity depletion and sharpness are not necessarily relevant, and so we have not included them in Tables 5 and 6. We have instead listed the mean, median, and maximum values. The maximum poleward depletion is of particular interest, as it is likely to represent a case with very few

TABLE 4
CAVITY MORPHOLOGIES

Data Set	Width at 1.2 $R_{\odot}$ (deg latitude)	Height ($R_{\odot}$)	Center (deg to equator)
Set 1: 12 primary.....	6/18/36	1.25/1.47/1.60	5/56/77
Set 2: 7 primary.....	4/12/22	1.24/1.37/1.58	17/32/50
Set 1 + Set 2: 19 primary....	4/16/36	1.24/1.43/1.60	5/47/77
Set 1 + Set 2: all 98 days....	4/18/40	1.24/1.46/1.64	5/54/90

NOTE.—All values are min/mean/max.

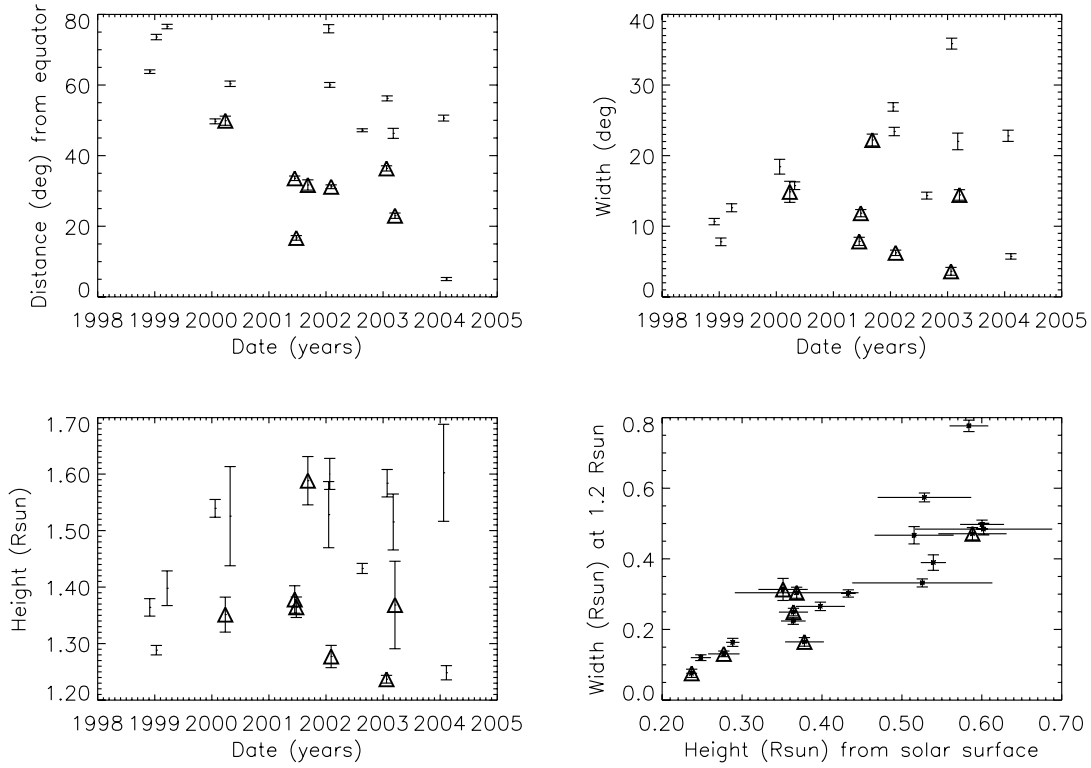

FIG. 6.—Center, angular width (at 1.2 $R_\odot$), and height vs. time, and linear width (at 1.2 $R_\odot$) vs. height (from solar surface) for the 19 primary days of cavity observations. Set 2 cavities are indicated as triangles.

if any intervening bright structures. This maximum value occurs for cavity 14, as observed on 2001 May 15, which had a poleward depletion of 43%. This cavity also possessed the largest value of cavity sharpness. In general, the darker the cavity is, the sharper its boundaries are: we demonstrate this by fitting straight lines to the data, as shown in Figure 7. The slopes of such lines are uniformly positive, whether we fit the line to the entire data set of combined sets 1 and 2 or to set 1 or set 2 independently. The equatorward sharpness and depletion have no such correlation, most likely due to the spurious effects of unrelated structures along the line of sight. Figure 7 and Tables 5 and 6 show that set 2 cavities tend to be less depleted and have less sharp boundaries than the set 1 cavities. This is not surprising, since the set 1 cavities were chosen for their visibility: most are PCFs, so that they are relatively large, positioned at high latitudes away from obscuring active regions, and oriented more or less along the line of sight so that cavity sharpness and depletion are not obscured by the angled cavity's own rim. The exception is cavity 14, which is both the darkest and most sharply defined cavity in our sample. However, it is quite a small cavity (7°.86 wide and 1.38 $R_\odot$ high), which also affects its overall visibility and explains why it was not chosen as a set 1 case. We discuss cavity 14 further in § 4.2.

TABLE 5
CAVITY DEPLETION

Data Set	Depletion: Equatorward	Depletion: Poleward
Set 1: 12 primary.....	0.27/0.24/0.47	0.16/0.17/0.34
Set 2: 6 primary.....	0.34/0.31/0.58	0.10/0.04/0.43
Set 1 + Set 2: 18 primary.....	0.29/0.28/0.58	0.14/0.12/0.43
Set 1 + Set 2: 75 days.....	0.27/0.25/0.58	0.14/0.12/0.43

NOTES.—Depletion is the fractional decrease of minimum cavity intensity as compared to rim cavity intensity. All values are mean/median/max. We include the median because of the strong influence of the outlier case of cavity 14 on the set 2 poleward mean.

These tables and figures only present information for the lower height (1.2 $R_\odot$). Since each cavity has a different second height, it would not be very meaningful to compare the information at the second height among all the cavities. However, because it is a relative quantity, it is interesting to consider how each cavity's depletion changes between the two heights. When we fit straight lines to Figure 8, we find that the poleward cavity depletion, which is the most trustworthy, as we have discussed, is reduced by 17% ± 7% between the lower and upper heights, which is a small but perhaps significant difference, implying that the density may drop off radially within the cavities at a rate somewhat less than the rate within their surrounding bright rims. If we make this calculation using only set 1 cavities, this reduction changes to 15% ± 8%, and if we use only set 2 cavities, it becomes 15% ± 9%.

4. CAVITIES THAT ERUPT AS CMEs

The differences in morphological and contrast properties discussed in § 3 between data sets 1 and 2 are due to the different ways that these data sets were selected. By first looking only for best-case cavities, we introduced a bias toward large, dark, sharp-edged cavities in set 1. By backtracking from three-part CMEs, we were able to identify the CME-producing cavities of set 2, which might otherwise have escaped our notice because they were small or did not contrast strongly with the surrounding corona. We emphasize, however, that cavities from both data sets erupted as CMEs.

4.1. *CMEs from Set 1*

Reviewing Table 2, we see that of the 12 set 1 cavities, nine could be associated with one or more CME at some time in their

TABLE 6
CAVITY SHARPNESS

Data Set	Sharpness: Equatorward	Sharpness: Poleward
Set 1: 12 primary	2.5E−8/3.1E−8/3.9E−8	1.8E−8/1.7E−8/4.2E−8
Set 2: 6 primary	3.5E−8/2.7E−8/9.1E−8	2.6E−8/8.6E−9/1.1E−7
Set 1 + Set 2: 18 primary	2.9E−8/2.7E−8/9.1E−8	2.0E−8/1.3E−8/1.1E−7
Set 1 + Set 2: 75 days	2.2E−8/1.9E−8/9.1E−8	1.4E−8/1.1E−8/1.1E−7

NOTES.—Sharpness is slope at cavity edge ($B_\odot$ deg^{-1}). All values mean/median/max. We include the median because of the strong influence of the outlier case of cavity 14 on the set 2 poleward mean.

lifetime (e.g., Fig. 9). Two of the other cases (cavities 3 and 11) were plagued with missing data, so it is impossible to say whether a CME occurred or not. The final case (cavity 7) was a curved filament that could only be clearly connected to a cavity for 2 days of observations before disappearing around the west limb, where it may have been associated with a back-side CME. As Table 2 shows, the visibility of all of the curved or angled filaments tended to be short lived, because their orientation to the line of sight changed as they rotated past the limb. (On the other hand, Fig. 10 shows that the only non-PCF-related case in set 1 [cavity 12] actually led to two cavities simultaneously visible at the east limb because of the circular nature of its associated filament!)

The fact that so many of our set 1 cavities erupted is perhaps not surprising. We were able to observe most of them for days: as many as 9 days at the limb in a row for longitudinally extended cases such as cavity 8 (Fig. 3), and recurrences at opposing limbs for up to 8 months, as in the case of cavity 4. Given that much time, most filaments tend to erupt eventually. Figure 9 shows one such case, on 1999 November 19. This was one of three CMEs observed by Mk4 associated with cavity 4. It is not uncommon for a PCF to partially erupt, leaving some or most of the extended filament and channel intact after the eruption. The cavities exhibit similar behavior, with both the filament and cavity visible again by the time they rotate to the opposing limb (see Fig. 11).

At least 12 CMEs were associated with the set 1 cavities at some time during their lifetimes. Of these we exclude three, because they occurred more than 24 hr from when a cavity was observed by Mk4 at the limb, specifically, cavities 1, 10, and 12. Because of Mk4 data dropouts at night, only five out of the remaining nine CMEs that we associated with set 1 were directly observed by Mk4. Table 7 lists these cases along with those observed to erupt by LASCO or EIT.

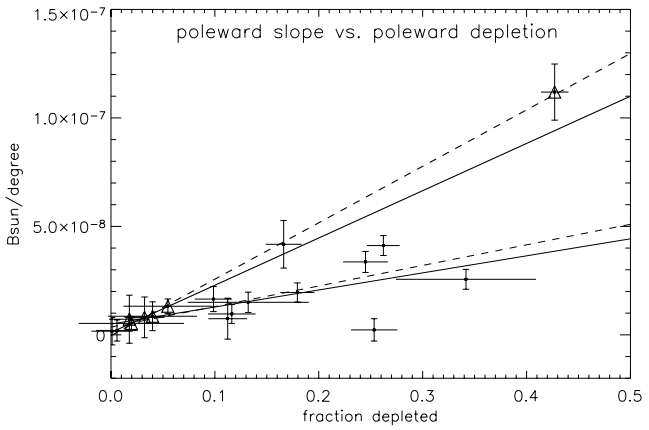

FIG. 7.—Poleward sharpness vs. poleward depletion for 18 of the 19 primary days observed. Set 2 cavities are indicated as triangles. The dashed thin line is a fit to all of the points shown; the solid thin line is a fit to all the points but cavity 14 (the outlier on the upper right). The dashed thick line is a fit just to set 2 data points (total of six points); the solid thick line is a fit to all set 2 points except cavity 14. (Note that a fit to just set 1 points produces a line essentially the same as the solid thin line, i.e., the fit to all data points but cavity 14.)

4.2. *CMEs from Set 2*

Our secondary data set, set 2, provides us with seven more examples of quiescent cavities erupting as CMEs, shown in Table 8. Four of these were observed in eruption by Mk4. Both Tables 7 and 8 list the linear fit velocity determined using LASCO observations, where available. The CMEs associated with set 2 cavities were significantly faster than those associated with set 1 cavities. Specifically, set 1 cavities had an average speed of 429 km s^{-1} (median of 389 km s^{-1}), and set 2 cavities had an average speed of 884 km s^{-1} (median of 901 km s^{-1}). This is at least partly due to the fact that the CMEs from set 1 were large-scale PCF eruptions, while the CMEs associated with set 2 were in many cases in close proximity to ARs, which usually produce faster CMEs (Gosling et al. 1976; Sheeley et al. 1999).

The fastest CME from either data set occurred on 2001 May 15 (set 2, cavity 14), which reached a velocity of 1280 km s^{-1}. The kinematics of this particular case has been analyzed by Vrsnak et al. (2004), who found highly correlated behavior between the soft X-ray flare and the acceleration of the CME. It may be significant that despite the general trend for set 2 data set cavities to be less dark and sharp edged than those of set 1, cavity 14 had the highest degree of cavity depletion and edge sharpness of the entire combined data sets. We discuss possible connections between cavity darkness and boundary sharpness and stored magnetic energy further in § 5.

4.3. *Properties of Erupting Cavities*

We are now in a position to consider how observations of cavities that will imminently erupt as CMEs are distinguished from the general set of cavity observations. In order to do this, we split

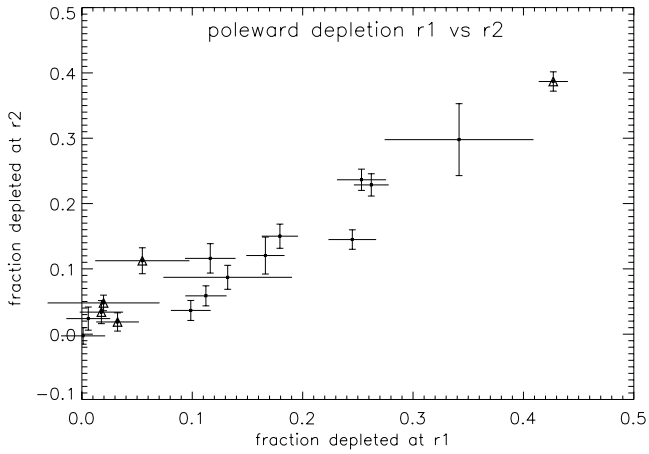

FIG. 8.—Poleward depletion at lower vs. higher heights for each primary cavity. Set 2 cavities are indicated as triangles.

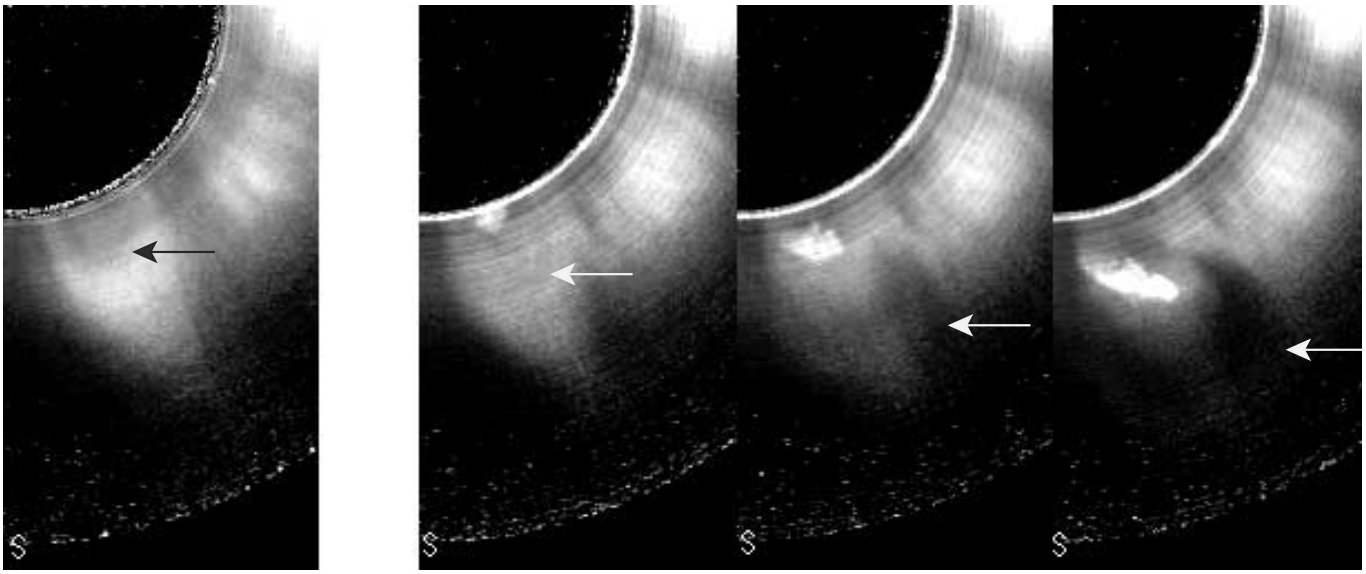

FIG. 9.—Quiescent cavity that erupts as CME, as observed by MLSO Mk4. *Left:* quiescent cavity on 1999 November 18. *Right three images:* CME erupting on 1999 November 19. [*This figure is also available as an mpeg animation in the electronic edition of the Astrophysical Journal.*]

our complete data set into three categories listed in Table 9: all days with cavity observations greater than 48 hr from any cavity-related CME (74 out of 98), all days with cavity observations where a CME does occur within 48 hr (24/98), and all days for which we had Mk4 observations of quiescent cavities that erupted within 24 hr (14/98).

4.3.1. *Morphology*

Historically, cases have been found in which a quiescent cavity was observed to gradually rise, swell, and ultimately be released in a CME (Fisher & Poland 1981; Illing & Hundhausen 1985; Hundhausen 1999; Srivastava et al. 1999). This is part of the same phenomenon of streamers swelling before eruption (Hundhausen 1993). It is also likely to be associated with a trend for filaments to be more likely to erupt in a CME if they extend high enough up in the corona (between 1.2 and 1.35 $R_{\odot}$ and thus visible above the occulter in the Mark IV coronameter; Munro et al. 1979; Zirin 1988, p. 267; Gilbert et al. 2000).

We therefore considered whether cavities appeared more swollen in the time leading up to the CME and whether or not a filament extended high enough to be visible in white light. Specifically, we looked for a property that we call "necking," that is, cavities whose angular widths decreased as they approached the occulting disk. Figure 12 shows examples of such necking cavities, both in white light and in EUV (*left and middle*), and also an example of a cavity with a visible white-light filament (*right*). We found that cavities that did not appear to neck in white light above the occulting disk often did when they could be observed all the way down to the disk in EUV. For this reason, we resisted calling this morphological feature "bulging" or "swelling," which might imply a structural change in the cavity, when it seems likely that necking occurs in the white-light data when a cavity having a more-or-less O-shaped cross section rises high enough so that its central axis lies above the occulter. Such an O-shaped cross section has important implications for the magnetic structure of the cavity, which we discuss below.

Table 9 illustrates that observations of cavities just prior to CMEs are more likely to exhibit necking in white light and have a filament high enough to be visible in white light above the occulter. Indeed, 12/14 of cavities that erupted in a CME within 24 hr exhibited clear necking in white light, as opposed to only 14/74 of the cavities observed more than 48 hr prior to CMEs, and 7/14 of them had a high white-light filament, as opposed to only 13/74 of the non-CME cavities. Both of the two same-day cases without clear necking had an angular width that appeared straight up and down at the occulting disk, which we classify as "indeterminate necking." Moreover, one had a white-light filament visible, and the other (cavity 6) was an exceptionally large cavity overlying a PCF oriented mainly parallel to the southern limb, and so perpendicular to the line of sight. We

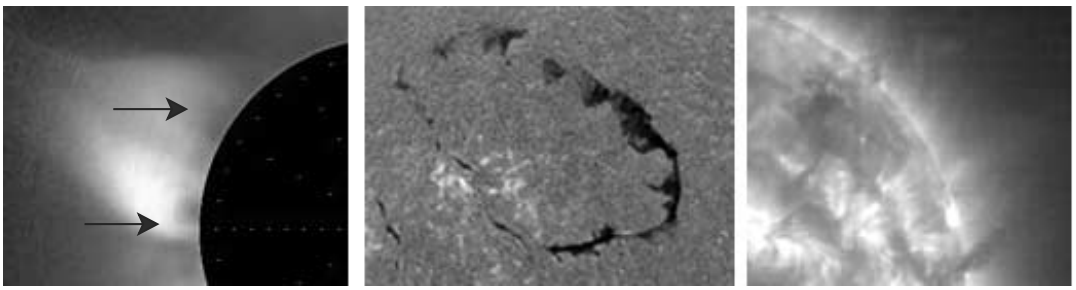

FIG. 10.—Circular filament: cavity 12. *Left:* Two cavities appear in Mk4 data when both the top and the bottom portions of the filament channel are oriented along the line of sight at the east limb (lower cavity is the one analyzed on 2004 January 10 in this paper). *Center:* Filament is seen on the disk as a squashed circle (2004 January 16; BBSO Hα). *Right:* EIT witnesses the filament erupting as a CME at the west limb on 2004 January 21, but the orientation of the filament at the limb is perpendicular to the line of sight, so no clear cavity is visible in Mk4. [*This figure is also available as an mpeg animation in the electronic edition of the Astrophysical Journal.*]

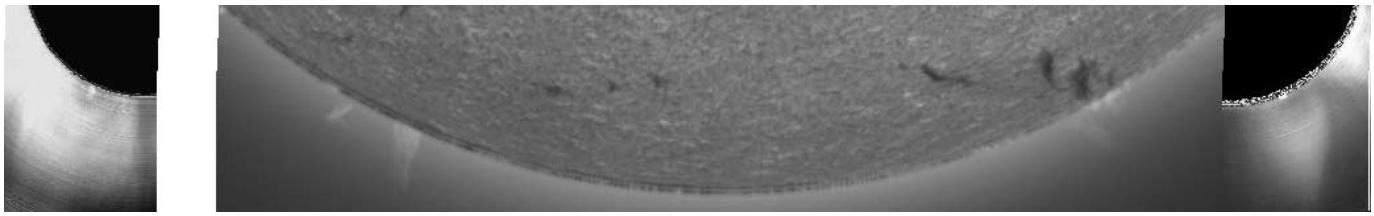

FIG. 11.—Example of cavity (cavity 4) and its associated filament reforming after an eruption. *Left:* Mk4 image of cavity with filament at east limb immediately before eruption, on 2000 March 3. *Right two images:* BBSO Hα image of PCF with filament present at west limb, visible also in the cavity observed by Mk4, on 2000 March 15.

might expect the cross section of a cavity to be broadened in such a case.

We also found individual cavities that showed an increase in cavity height, degree of necking, and presence or increase of height of filament in the days leading up to the CME. Figure 13 shows an example for the cavity that erupted as a CME (observed by LASCO and EIT) on 2002 July 23 (cavity 8). On July 21, although the cavity was clear, there was no evidence for necking or a white-light filament. On July 22, the day before the eruption, the cavity was higher and both necking and a white-light filament were present. It is impossible to know whether this change was caused by a true evolution, e.g., a rising cavity, or whether the Sun simply rotated a higher portion of the three-dimensional cavity into the line of sight. We need multiple lines of sight, such as will be available when we combine Mk4 observations with those from the Solar Terrestrial Relations Observatory (STEREO) Coronagraph 1 (COR1) instrument, to make such distinctions. However, it is worth noting a similar evolution on a longer time frame, as shown by Figure 14. The evolution of cavity 4 is shown, demonstrating that its height increased steadily as it rotated past opposing limbs, reaching a maximum height the day before it erupted in a CME on 1999 November 19. Since these observations were of the days that the cavity was most visible at each limb, it is reasonable to deduce that there was a true, gradual slow rising of the cavity with time rather than the combined effects of line-of-sight projection and rotation.

4.3.2. *Contrast*

We also considered whether cavities observed on days near CMEs were darker or had sharper boundaries than those observed on days not near cavity-related CMEs. Set 2 cavities tend to have smaller depletion and sharpness than the set 1 cavities that make up the majority of observed days, but this is due to selection effects discussed above. Indeed, all of the noCME48 cases listed in Table 9 are from set 1, so it is most appropriate to only compare those cavity observations within 48 hr and 24 hr, respectively, that arise from set 1 to the noCME48 cases. If we compare only cavities from set 1 observed within 24 hr of CMEs to set 1 observations greater than 48 hr from a CME, we find that the same-day CME cases have on average 45% steeper poleward edges and 14% greater poleward depletion (see Table 10). Another approach is to look at the evolution of these contrast properties prior to the CME. In the case shown in Figure 13, the poleward cavity depletion has increased by 27% from July 21 to July 22, and the poleward edge sharpness by 71%. These results should be treated with caution: it is possible that we are biassed toward CMEs occurring near the limb, so that associated precursor cavities would tend to also be closer to the limb than the general population, and thus be more clearly visible. This question should be revisited with a more systematic data set in future, in order to establish whether it is possible that increased cavity darkness and sharpness imply increased likelihood of CMEs. This will be discussed further in § 5.

4.4. *Bodily Eruption of Cavities*

Finally, we address the question that motivates this entire study: do cavities erupt bodily as CMEs? By "bodily erupt," we mean that the pre-CME cavity appears to lift off in the eruption without significant change to its morphology. We have many examples of cavities that erupt as CMEs, but we require Mk4 observations of the actual eruptions to directly connect the quiescent cavity to the erupting cavity. Some of the Mk4 observations of cavity-related CMEs begin at times when the CME is already in progress; these are indicated in Tables 7 and 8 with footnote a. The events of greatest relevance to this question are those in which Mk4 observes a quiescent cavity that begins its eruption some time into the day's observations. We have found four such cases, both PCF-related eruptions from set 1 and smaller, AR-associated

TABLE 7
CMEs FROM SET 1

Date	Cavity	Observed by	Speed (km s^{-1})
1998 December 19	2	Mk4[a]	N/A
1999 February 5	2	Mk4	660
1999 November 19	4	Mk4[a]	N/A
1999 December 29	5	LASCO/EIT	340
2000 February 5	4	Mk4	389
2000 March 3	4	Mk4[a]	334
2001 December 22	6	EIT	N/A
2002 July 23	8	LASCO/EIT	423
2003 January 1	9	EIT	N/A

NOTE.—All speeds from LASCO CME catalog, if available: http://cdaw.gsfc.nasa.gov/CME_list.
[a] Already erupting when Mk4 begins observing.

TABLE 8
CMEs FROM SET 2

Date	Cavity	Observed by	Speed (km s^{-1})
2000 February 26	13	LASCO/EIT	668
2001 May 15	14	Mk4	1280
2001 May 25	15	Mk4[a]	930
2001 August 9	16	Mk4	909
2002 January 4	17	LASCO/EIT	896
2002 December 28	18	LASCO/EIT	901
2003 February 16	19	Mk4	603

NOTE.—All speeds from LASCO CME catalog, if available: http://cdaw.gsfc.nasa.gov/CME_list.
[a] Already erupting when Mk4 begins observing.

TABLE 9
PROPERTIES OF ERUPTING CAVITIES

Quantity	noCME48	CME48	CMESD
Total number	74	24	14
Percent visible white-light filament (%)	18	46	50
Percent necking (%)	19	54	86
Percent necking indeterminate (%)	34	42	14
Percent no necking (%)	47	4	0

NOTE.—noCME48 cases are days with cavity observations more than 48 hr from related CME, CME48 cases are days with cavity observations within 48 hr of related CME, and CMESD cases are days with cavities erupting within 24 hr.

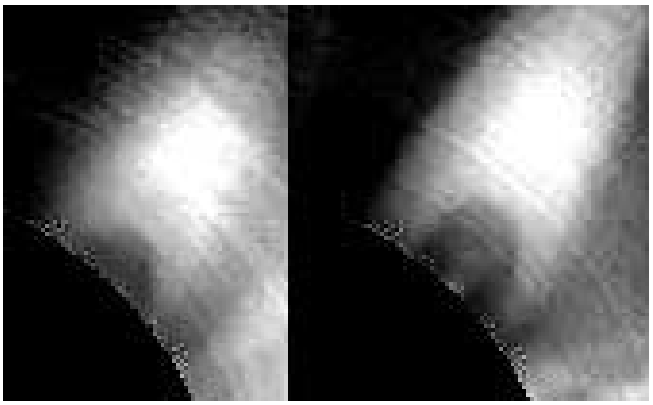

FIG. 13.—Mk4 observations of rising cavity (cavity 8), with filament and necking becoming apparent. *Left:* 2002 July 21. *Right:* 2002 July 22.

eruptions from set 2: specifically, 1999 February 5, 2000 February 5, 2001 May 15, and 2001 August 9 (cavities 2, 4, 14, and 16). These, along with the previous examples discussed above (Fisher & Poland 1981; Illing & Hundhausen 1985; Hundhausen 1999; Srivastava et al. 1999; Maricic et al. 2004), are "smoking guns" that demonstrate that quiescent cavities can erupt bodily as a CME.

Figures 15 and 16 show time sequences of examples of set 1 and set 2 cases, respectively. The CME of 1999 February 5 was visible as a quiescent cavity, possessing a white-light filament and necking, from 17:49 to 18:27 UT, at which point it began to rise and erupt. It appeared to erupt bodily, with no qualitative change to the cavity and its filament except for their rise and expansion outward. Similarly, the CME of 2001 August 9 was visible as a quiescent cavity, possessing a white-light filament and necking, from 16:56 to 19:50 UT. During this time there was a very slow, gradual rising as well as an enhancement of cavity contrast and necking, culminating in a clear upward eruption at 19:50 UT. Again, the cavity and its associated filament appeared to bodily erupt in the CME at this time.

5. IMPLICATIONS FOR THE MAGNETIC STRUCTURE OF CMEs AND THEIR PRECURSORS

5.1. *Theoretical Background*

It is widely agreed that the ultimate energy source for CMEs lies in coronal magnetic fields. CMEs occur on dynamic timescales that are much shorter than that of observed photospheric motions, which implies that they are powered by the release of stored energy (Low 1996). Direct information about coronal magnetic fields has proved elusive to date, as routine and comprehensive coronal magnetic field observations are only now beginning to become available (Lin et al. 2004; Tomczyk 2004). However, observations of photospheric vector magnetic fields have long shown that nonpotential magnetic fields are common (Hagyard et al. 1984; Leka et al. 1996), and observations of coronal plasma structures exhibit a degree of complexity and shear that strongly indicates a nonpotential quiescent coronal magnetic field. This nonpotentiality in turn implies the presence of free magnetic energy that may be tapped to drive coronal dynamic phenomena.

The exact nature of the pre-CME energized magnetic field is an important constraint on models of CME initiation. One attractive possibility is that the magnetic fields take the form of a magnetic flux rope of twisted field lines winding about an axial field line. A variety of models describe the CME in eruption as a flux rope and demonstrate that this magnetic topology gives rise to a three-part structure (Chen 1996; Gibson & Low 1998, 2000; Guo & Wu 1998; Lynch et al. 2004). Many of these models also demonstrate that essentially the same physical reasons for the presence of the three-part structure in eruption hold true in quiescence when the pre-CME magnetic configuration is also that of a flux rope. The sharply defined cavity arises in these models from the flux rope configuration, possessing strong internal magnetic pressure and winding field lines that are partially detached from the photosphere; the prominence core material is supported by the dipped portion of the thermally isolated winding field, and the front or helmet streamer is the interface between the flux rope system and surrounding, more simply sheared arcade field (Low & Hundhausen 1995; Low 1996; see Fig. 17).

The idea of the erupting CME as a magnetic flux rope has gained acceptance over the years (Amari et al. 2003; Chen & Krall 2003; Roussev et al. 2003; MacNeice et al. 2004; Manchester et al. 2004). Moreover, CMEs have been related to interplanetary counterparts, known as magnetic clouds, which are often modeled as magnetic flux ropes (Burlaga et al. 1982; Burlaga 1988).

FIG. 12.—*Left and middle:* Examples of "necking," cavities whose angular widths decrease as they approach the solar occulter (white light) or solar limb (EUV). *Right:* Example of cavity containing filament (prominence) visible in white light (note that necking is indeterminate in this case). White-light images are Mk4 observations of 1999 December 26 (cavity 5; *left*) and 2000 March 27 (cavity 4; *right*). *SOHO* EIT image is of 2002 December 27 (cavity 18; *middle*).

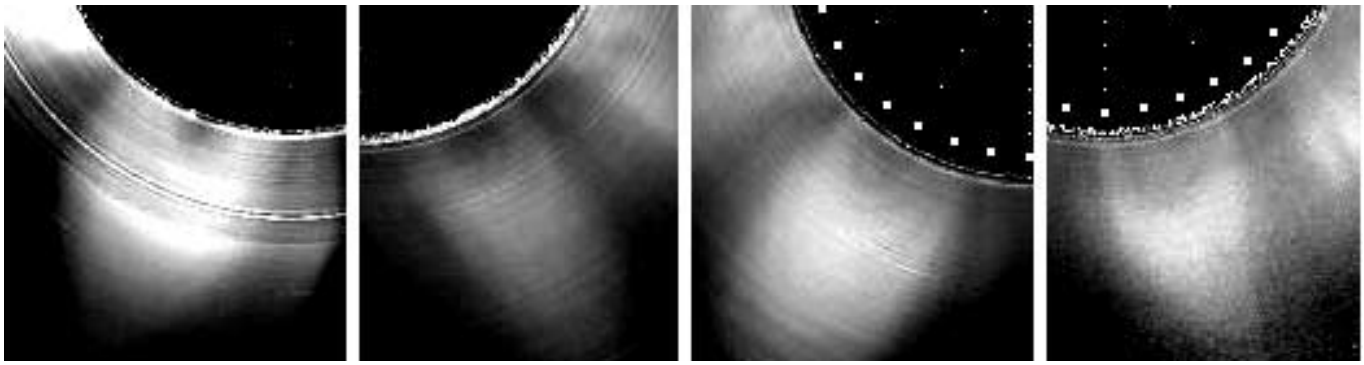

FIG. 14.—Mk4 observations of long-term evolution of a rising cavity (cavity 4). *Left to right:* 1999 October 1, 1999 October 19, 1999 November 2, and 1999 November 18.

However, the question of whether the flux rope is formed during the eruption or whether the flux rope existed prior to the eruption remains controversial (Amari et al. 2003). Why does the presence or absence of a precursor magnetic flux rope matter? Flux ropes are not theoretically required to drive CME eruption: for example, the "breakout model" (Antiochos et al. 1999a), which has an initial coronal magnetic configuration that is highly sheared and complex, but not a flux rope, is a case in which the flux rope forms during the eruption. We submit that there are two reasons why the presence of a flux rope prior to eruption is of interest.

First of all, it has implications for the nature of magnetohydrodynamic equilibria in the quiescent corona. It has been suggested that magnetic flux ropes are fundamental building blocks of coronal magnetism (Rust 2003). Taylor (1974) demonstrated that in a finite domain system that conserves global magnetic helicity during reconnection, the minimum energy state is that of a linear force-free field. The corona is unlikely to obtain a truly linear force-free magnetic field (Antiochos et al. 1999a; Low 1999), but will tend toward metastable equilibrium states that minimize energy while preserving helicity. Magnetic flux ropes may then be of import as a standard metastable equilibrium state in the quiescent corona for regions that possess significant helicity (Low 1996, 2001).

Second, a preeruption flux rope has implications for the physics of CME initiation. A range of models have demonstrated how CMEs can arise from an initial flux rope configuration (see, e.g., Forbes 2000 and references therein). The preeruption flux rope intrinsically contains the energy required to propel it outward in a CME. As an equilibrium state it is likely to be temporary, so that as conditions change within and around the flux rope, the equilibrium is eventually lost, and the rope expends its stored magnetic energy and erupts outward as a CME (Linker et al. 2003; Fan 2006).

5.2. *Relevance of Cavity Observations to Magnetic Flux Rope Controversy*

Perhaps the most compelling reason to model the presence and ultimate loss of coronal magnetic equilibria in terms of magnetic flux ropes, however, is that such models match observations well. This is largely why magnetic flux rope models have been applied to solar regimes from the interior out to 1 AU, matching observations of emerging twisted flux (Tanaka 1991; Leka et al. 1996; Lites et al. 1995), apparent shear/rotational motions at the photosphere (Lopez Fuentes 2000; Green et al. 2002; Mandrini et al. 2005; Gibson et al. 2004), observed properties of coronal prominences (Priest et al. 1989; Rust 1994; Rust & Kumar 1994; Lites & Low 1997; Gibson & Low 1998; Aulanier & Démoulin 1998), X-ray sigmoids (Rust & Kumar 1994; Titov & Démoulin 1999; Low & Berger 2003; Fan & Gibson 2003, 2004; Kliem et al. 2004; Gibson et al. 2004), and three-part CMEs and magnetic clouds, as referenced above. Observations of quiescent cavities have also long been considered evidence of flux ropes existing in the corona prior to eruption (Low 1994), and recent observational case studies have explicitly supported this conclusion (Yurchyshyn 2002; Maricic et al. 2004; Vrsnak et al. 2004).

Our observational survey of quiescent white-light cavities provides further detailed and extensive support for the premise of equilibrium magnetic flux ropes existing in the corona prior to their eruptions as CMEs. The flux rope model gives rise to the cavity as a thermally isolated, magnetically confined region of depleted density. When long, sheared field lines such as those within the flux rope are subjected to enhanced, localized footpoint heating, prominence material can condense in field line dips (Antiochos & Klimchuk 1991; Antiochos et al. 1999b). Because the flux rope field winds more than a full turn about the

TABLE 10
PROPERTIES OF ERUPTING CAVITIES: SET 1 ONLY

Quantity	noCME48	CME48	CMESD
Equatorward depletion	0.03/0.25/0.54	0.08/0.28/0.42	0.08/0.30/0.42
Poleward depletion	0.00/0.14/0.34	0.06/0.15/0.26	0.10/0.16/0.26
Equatorward sharpness	2.1E−9/1.9E−8/4.1E−8	5.4E−9/2.8E−8/6.7E−8	1.3E−8/2.5E−8/4.3E−8
Poleward sharpness	3.4E−10/1.3E−8/4.9E−8	6.1E−9/1.6E−8/4.1E−8	9.6E−9/1.9E−8/4.1E−8

NOTES.—noCME48 cases are days with cavity observations more than 48 hr from related CME, CME48 cases are days with cavity observations within 48 hr of related CME, and CMESD cases are days with cavities erupting within 24 hr. Depletion is the fractional decrease of minimum cavity intensity as compared to rim cavity intensity. Sharpness is in units $B_\odot$ per degree polar angle. All values are min/mean/max.

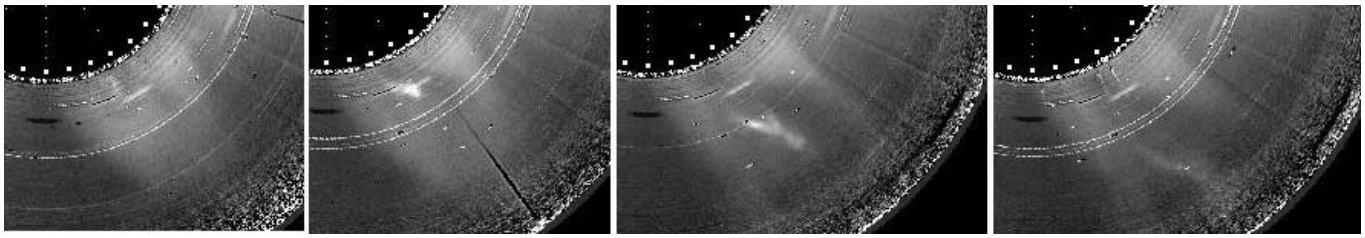

FIG. 15.—Mk4 observations of eruption of quiescent cavity (cavity 2) on 1999 February 5. *Left to right:* 17:58 UT, 20:20 UT, 21:24 UT, and 22:10 UT. [*This figure is also available as an mpeg animation in the electronic edition of the Astrophysical Journal*.]

rope axis, plasma lying on the field lines between the dips will be thermally isolated from the photosphere, so that a magnetically confined, depleted cavity can exist until such an equilibrium is lost. The circular cross section of the flux rope gives rise to the circular cross section of the cavity that is so nicely demonstrated by our observed cavities with the property we have called "necking." Moreover, the magnetic flux surface at the boundary between the rope and surrounding fields gives rise to the sharp cavity boundary (Low 1996, 2001). The gradual rising and swelling of a cavity prior to its eruption discussed in § 4.3.1 is consistent with the progression of a flux rope through a sequence of quasi-static equilibria as it emerges from beneath the photosphere and rises into the corona (Wolfson et al. 1987; Fan & Gibson 2004, 2005; Fan 2006). An increase in cavity darkness and edge sharpness prior to eruption as discussed in § 4.3.2 could also be a manifestation of a slowly rising flux rope, either because as it rises a darker, more sharply defined portion of the structure has moved into the line of sight, or because the rising rope has become more energized as it rises, resulting in the magnetic confinement of a more depleted (and thus more magnetically buoyant) cavity. Such an energization of the flux rope might continue until a threshold is reached where equilibrium is no longer possible, so that an eruption necessarily ensues.

Such arguments demonstrate that a magnetic flux rope is sufficient to explain our observations of quiescent cavities, but is it necessary? It is true that the expansion of any sheared magnetic field, whether it emerges from below the photosphere already sheared or whether it is sheared in the corona by photospheric footpoint motions, could create a region of depleted density. However, without the thermal detachment of the portion of the rope field between the prominence-mass-filled dips of the rope, the expanded region would refill from below on timescales much shorter than that of the cavity's lifetime, which as we have shown is certainly on the order of days and probably is as long as weeks or even months. Dipped, prominence-mass-containing field can exist in a sheared, non-flux-rope field (Antiochos et al. 1994), but the circular cross section of the cavity and sharp boundary consistent with a magnetic flux surface imply an organization of the magnetic field's shear that is most simply obtained in a flux-rope-type field configuration. We have, admittedly, selected for cavities possessing such circular cross sections and sharply defined boundaries, and more amorphous, less well defined regions of density depletion also exist that may be explained by non-flux-rope magnetic topologies (Antiochos et al. 1999b). However, we have demonstrated direct links between the clearly defined cavities studied here and CMEs, and the morphology and persistence of these pre-CME cavities are best explained by magnetic flux rope models. This then is evidence for the existence of pre-CME flux ropes in the corona.

6. CONCLUSIONS

We have undertaken the first comprehensive study of coronal white-light cavities in order to gain information about the state of the corona prior to CMEs. We find, first of all, that such cavities are ubiquitous. We have analyzed only a fraction of the total number of quantifiable cavities present in the Mk4 data set, and the number of cavities the Mk4 telescope observes represents a lower limit on the number actually present, since only cavities that are high enough, dark enough, and without significant obscuring features along the line of sight will appear in the white-light coronagraph images. The ubiquity of cavities is a direct consequence of the ubiquity of filaments, because the cavities are simply those filament channels that extend high enough to be observed in occulted coronal limb images. White-light cavities are most easily seen in polar crown filaments, but we have demonstrated here that they also exist in lower latitude filaments associated with active regions.

The PCF-related cavities (e.g., set 1) tend to be larger, centered at higher latitudes (not surprisingly), and often visible for many days. We have found PCF-cavity cases that are visible for as many as 9 days at one limb, and when the reappearances of the cavity on opposing limbs are considered, we have found cavities that last for as long as 8 months. We also find that CMEs associated with our set 1 PCF-related cavities tend to be slower than

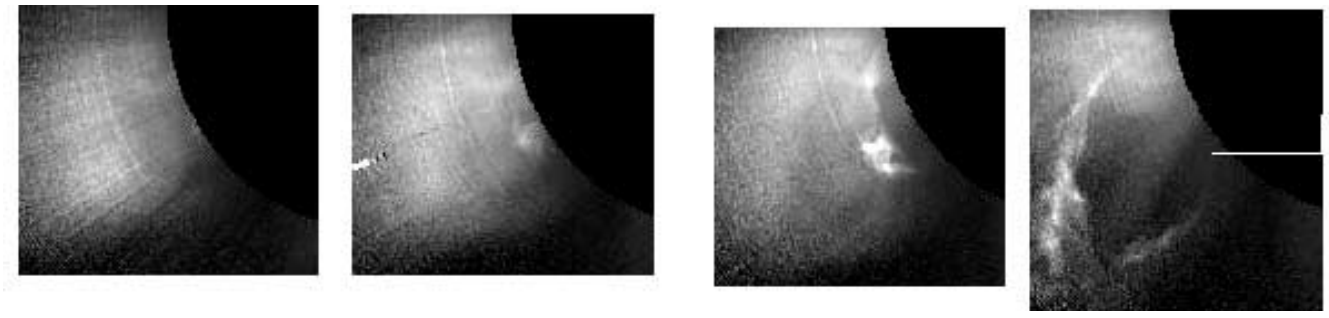

FIG. 16.—Mk4 observations of eruption of quiescent cavity (cavity 16) on 2001 August 9. *Left to right:* 16:59 UT, 20:18 UT, 20:51 UT, and 21:29 UT. [*This figure is also available as an mpeg animation in the electronic edition of the Astrophysical Journal*.]

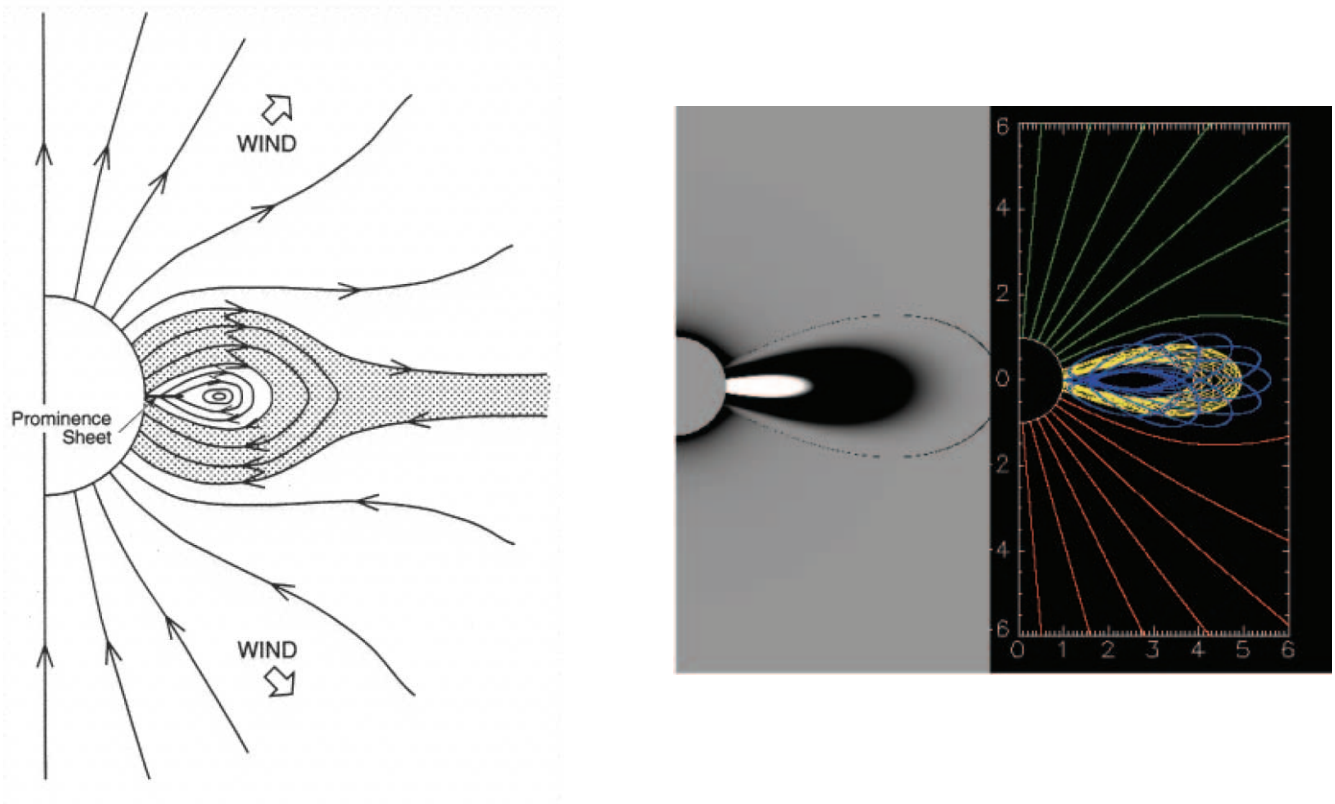

FIG. 17.—*Left:* Magnetic flux rope model of CMEs and quiescent cavities (Low & Hundhausen 1995). *Right:* Gibson & Low (2000) quantitative MHD model prediction of coronal white-light intensity (*pB*; *left*) and magnetic field lines (*right*).

those of set 2. This illustrates an important consequence of selecting cavities based on visibility. A cavity is most visible when it is large and elongated, lies away from obscuring structures, and is oriented along the viewer's line of sight. Smaller cavities, cavities lying along sheared neutral lines, and cavities lying in the midst of active regions will tend to be less visible, and these very factors that reduce their visibility may increase their likelihood of producing, on average, more highly energetic CMEs. By grouping our cavities based essentially on visibility, we obtained two physically distinct sets, one including cavities associated with older, high-latitude filament channels (set 1), and the other including cavities associated with younger filaments lying in the midst of active regions (set 2).

The commonalities between these distinct sets are very interesting, however. In quantifying the morphological and intensity contrast properties of our cavities, we find a significantly constant aspect ratio between cavity width and height that holds true for all cavities. This, in combination with the appearance of cavity "necking," is evidence for a common cavity morphology possessing an O-type cross section. We also find a correlation for all cavities between poleward intensity depletion and sharpness of the poleward edge of the cavity. Our data set suggests that the degree of intensity depletion within the cavities may decrease with height, which could indicate that the density drops off radially more slowly within cavities than in their surrounding bright rims. This may have implications for the magnetostatic force balance of the cavities. Alternatively, it could be a projection effect if, for example, the arcade loops surrounding the cavity contribute more to the line-of-sight integration with increasing height. Both morphological and MHD models need to be considered in conjunction with a larger statistical set of data to resolve this issue.

Although set 1 cavities possess larger intensity depletion and cavity sharpness on average than those of set 2, the case of maximum depletion and cavity sharpness was a set 2 cavity. The depletion at 1.2 $R_{\odot}$ within this cavity was 43%, but it is important to emphasize that this is an intensity depletion, dependent on a weighted integral of densities along the line of sight. Since set 2 cavities are more prone to the reduction of intensity depletion by structures along the line of sight, it is possible that both sets have similar actual cavity density depletions. In order to investigate this more completely, we have begun detailed studies using three-dimensional morphological models based on those of Gibson et al. (2003) to examine how cavity visibility is likely to depend on cavity size, neutral line orientation, and other line-of-sight projection effects (see also Cremades & Bothmer 2004 for a discussion on line-of-sight projection and neutral-line orientation effects). This will be the subject of a future paper.

We have found multiple cases of cavities erupting bodily as CMEs, including examples from both sets 1 and 2. As discussed above, this is evidence for the presence of magnetic flux ropes in the corona prior to the CME. Considering that many pre-CME cavities may be too small, too faint, too far off-limb, or too obscured by structures along the line of sight to be visible in white light prior to eruption, along with the fact that Mk4 only observed for part of each day (or less, depending on weather), the fact that we found nine cavity-to-CMEs directly observed by Mk4 and seven more implied cases between 1998 and 2003 indicates that they are not uncommon occurrences. Whether it is possible that all CMEs originate in some sort of cavity requires further analysis, preferably using the multiple lines of sight that will be available when Mk4 observations can be combined with those of the STEREO COR1 coronagraphs.

Although the PCF-related cavities in particular can be extremely stable and long lived, given enough time they do erupt, and often more than once. The fact that these cavities can erupt multiple times, and that cavities and their associated filaments will reappear along approximately the same portion of the filament channel within days of the eruption, implies that the CME has not completely removed their underlying magnetic structure. Partially erupting magnetic flux ropes, where a significant portion of the twisted field remains behind after the eruption, have been demonstrated numerically and used to explain partial filament eruptions and the quick reforming of X-ray sigmoids (Gibson & Fan 2006; Gibson et al. 2006). It seems likely that a similar phenomenon, although along elongated PCF cavities, is occurring here.

A particularly topical question is whether our study provides any information useful for the prediction of CMEs. Because they are often stable, equilibrium structures, the presence of a quiescent cavity is not by itself a good indicator of an impending CME. However, as one of the basic observables predicted by magnetic flux rope models, white-light cavities may identify regions having sufficient stored magnetic energy to drive CMEs. The evolution of these cavities just prior to the CME that we have observed, including necking, the rising of associated filaments, and possibly a darkening cavity with a more sharply defined boundary, not only may be useful for indicating when a region is about to erupt, but also may give us insight into the physics behind the eruption, which is ultimately our best route to significant improvements in CME prediction.

Finally, regardless of what magnetic model is proposed, these observations of quiescent cavities and their relation to CMEs place direct constraints on the nature of coronal equilibrium states and the origins of CMEs. In particular, models must quantitatively reproduce cavity intensity contrast and sharp edges, cavity sizes (heights/widths/lengths) and shapes (O type), cavity evolution prior to CMEs (necking, high filament, possibly darkening, and sharpening boundary), and perhaps most challenging, cavity longevity and stability. In order to achieve this, it is likely that the thermodynamic nature of filaments and filament cavities will need to be considered along with three-dimensional MHD models of their magnetic structure and evolution. While this is a challenging prospect, recent advances in both theoretical models and observations make it one that is likely to be well worth attempting.

We thank Tom Holzer for his internal HAO review of this paper and B. C. Low, Yuhong Fan, Mei Zhang, Tibor Toerok, and Chris St. Cyr for interesting discussions. *SOHO* is a project of international cooperation between ESA and NASA. This material is based on research sponsored by the Air Force Research Laboratory, under agreement F49620-02-0191. The National Center for Atmospheric Research is sponsored by the National Science Foundation.

REFERENCES

Amari, T., Luciani, J. F., Aly, J. J., Mikic, Z., & Linker, J. 2003, ApJ, 585, 1073
Antiochos, S. K., Dahlburg, R. B., & Klimchuk, J. A. 1994, ApJ, 420, L41
Antiochos, S. K., Devore, C. R., & Klimchuk, J. A. 1999a, ApJ, 510, 485
Antiochos, S. K., & Klimchuk, J. A. 1991, ApJ, 378, 372
Antiochos, S. K., MacNeice, P. J., Spicer, D. S., & Klimchuk, J. A. 1999b, ApJ, 512, 985
Aulanier, G., & Démoulin, P. 1998, A&A, 329, 1125
Billings, D. E. 1966, A Guide to the Solar Corona (New York: Academic)
Burlaga, L. F. 1988, J. Geophys. Res., 93, 7217
Burlaga, L. F., Klein, L., Sheeley, N. R., Jr., Michels, D. J., Howard, R. A., Koomen, M. J., Schwenn, R., & Rosenbauer, H. 1982, Geophys. Res. Lett., 9, 1317
Chen, J. 1996, J. Geophys. Res., 101, 27499
Chen, J., & Krall, J. 2003, J. Geophys. Res., 108, 1410
Cremades, H., & Bothmer, V. 2004, A&A, 422, 307
Elmore, D. F., Burkepile, J. T., Darnell, J. A., Lecinski, A. R., & Stanger, A. L. 2003, Proc. SPIE, 4843, 66
Engvold, O. 1989, in Dynamics and Structures of Quiescent Prominences, ed. E. R. Priest (Dordrecht: Reidel), 47
Fan, Y. 2005, ApJ, 630, 543
Fan, Y., & Gibson, S. E. 2003, ApJ, 589, L105
———. 2004, ApJ, 609, 1123
———. 2005, in Connecting Sun and Heliosphere, ed. B. Fleck & T. H. Zurbuchen (ESA SP-592; Noordwijk: ESA)
Fisher, R. R., & Poland, A. I. 1981, ApJ, 246, 1004
Forbes, T. G. 2000, J. Geophys. Res., 105, 23153
Gibson, S. E., & Fan, Y. 2006, ApJ, 637, L65
Gibson, S. E., Fan, Y., Mandrini, C., Fisher, G., & Démoulin, P. 2004, ApJ, 617, 600
Gibson, S. E., Fan, Y., Torok, T., & Kliem, B. 2006, in Solar Dynamics and its Effects on the Heliosphere and Earth (Berlin: Springer), in press
Gibson, S. E., Foster, D. J., Guhathakurta, M., Holzer, T., & St. Cyr, O. C. 2003, J. Geophys. Res., 108, 1444
Gibson, S. E., & Low, B. C. 1998, ApJ, 493, 460
———. 2000, J. Geophys. Res., 105, 18187
Gilbert, H. R., Holzer, T. E., Burkepile, J. T., & Hundhausen, A. J. 2000, ApJ, 537, 503
Gosling, J. T., Hildner, E., MacQueen, R. M., Munro, R. H., Poland, A. I., & Ross, C. L. 1976, Sol. Phys., 48, 389
Green, L. M., Lopez Fuentes, M. C., Mandrini, C. H., Démoulin, P., van Driel-Gesztelyi, & J. L. Culhane, 2002, Sol. Phys., 208, 43
Guo, W. P., & Wu, S. T. 1998, ApJ, 494, 419
Hagyard, M. J., Teuber, D., West, E. A., & Smith, J. B. 1984, Sol. Phys., 91, 115
Harvey, K. L., & Gaizauskas, V. 1998, in IAU Colloq. 167, New Perspectives on Solar Prominences, ed. D. Webb, D. Rust, & B. Schmieder (ASP Conf. Ser. 150; San Francisco: ASP), 269
Hudson, H. S., Acton, L. W., Harvey, K. A., & McKenzie, D. M. 1999, ApJ, 513, L83
Hudson, H., & Schwenn, R. 2000, Adv. Space Res., 25, 1859
Hundhausen, A. J. 1993, J. Geophys. Res., 98, 13177
———. 1999, in The Many Faces of the Sun: A Summary of the Results from NASA's *Solar Maximum Mission*, ed. K. T. Strong et al. (New York: Springer), 143
Illing, R. M., & Hundhausen, A. J. 1985, J. Geophys. Res., 90, 275
———. 1986, J. Geophys. Res., 91, 10951
Kliem, B., Titov, V. S., & Torok, T. 2004, A&A, 413, L23
Kundu, M. R., Fuerst, E., Hirth, W., & Butz, M. 1978, A&A, 62, 431
Leka, K. D., Canfield, R. C., McClymont, A. N., & van Driel-Gesztelyi, L. 1996, ApJ, 462, 547
Lin, H., Kuhn, J. R., & Coulter, R. 2004, ApJ, 613, L177
Linker, J. A., Mikic, Z., Lionello, R., Riley, P., Amari, T., & Odstrcil, D. 2003, Phys. Plasmas, 10, 1971
Lites, B. W., & Low, B. C. 1997, Sol. Phys., 174, 91
Lites, B. W., Low, B. C., Martinez-Pillet, V., Seagreaves, P., Skumanich, A., Frank, Z. A., Shine, R. A., & Tsuneta, S. 1995, ApJ, 446, 877
Lopez Fuentes, M. C., Démoulin, P., Mandrini, C. H., & van Driel-Gesztelyi, L. 2000, ApJ, 544, 540
Low, B. C. 1994, Phys. Plasmas, 1, 1684
———. 1996, Sol. Phys., 167, 217
———. 1999, Geophys. Monogr., 111, 25
———. 2001, J. Geophys. Res., 106, 25141
Low, B. C., & Berger, M. 2003, ApJ, 589, 644
Low, B. C., & Hundhausen, J. R. 1995, ApJ, 443, 818
Lynch, B. J., Antiochos, S. K., MacNeice, P. J., Zurbuchent, T. H., & Fisk, L. A. 2004, ApJ, 617, 589
MacNeice, P., Antiochos, S. K., Phillips, A., Spicer, D. S., DeVore, C. R., & Olson, K. 2004, ApJ, 614, 1028
Manchester, W. B., Gombosi, T. I., Roussev, I., De Zeeuw, D. L., Sokolov, I. V., Powell, K. G., Toth, G., & Opher, M. 2004, J. Geophys. Res., 109, A01102
Mandrini, C. H., Pohjolainen, S., Dasso, S., Green, L. M., Démoulin, P., van Driel-Gesztelyi, L., Copperwheat, C., & Foley, C. 2005, A&A, 434, 725
Maricic, D., Vrsnak, B., Stanger, A. L., & Veronig, A. 2004, Sol. Phys., 225, 337
Marqué, C. 2004, ApJ, 602, 1037
McCabe, M. K., & Mickey, D. L. 1981, Sol. Phys., 73, 59
McIntosh, P. S., Krieger, A. S., Nolte, J. T., & Vaiana, G. 1976, Sol. Phys., 49, 57

Munro, R. H., Gosling, J. T., Hildner, E., MacQueen, R. M., Poland, A. I., & Ross, C. L. 1979, Sol. Phys., 61, 201
Priest, E. R., Hood, A. W., & Anzer, U. 1989, ApJ, 344, 1010
Roussev, I. I., Forbes, T. G., Gombosi, T. I., Sokolov, I. V., DeZeeuw, D. L., & Birn, J. 2003, ApJ, 588, L45
Rust, D. M. 1994, Geophys. Res. Lett., 21, 241
———. 2003, Adv. Space Res., 32, 1895
Rust, D. M., & Kumar, A. 1994, Sol. Phys., 155, 69
Saito, K., & Hyder, C. 1968, Sol. Phys., 5, 61
Saito, K., & Tandberg-Hanssen, E. 1973, Sol. Phys., 31, 105
Schmahl, E. J. 1979, in IAU Colloq. 44, The Physics of Solar Prominences, ed. E. Jensen, P. Maltby, & F. Orrall (Oslo: Inst. Teor. Astrophys.), 102
Serio, S., Vaiana, G. S., Godoli, G., Motta, S., Pirronello, V., & Zappala, R. A. 1978, Sol. Phys., 59, 65
Sheeley, N. R., Walters, J. H., Wang, Y.-M, & Howard, R. A. 1999, J. Geophys. Res., 104, 24739
Srivastava, N., Schwenn, R., & Stenborg, G. 1999, in 8th *SOHO* Workshop: Plasma Dynamics and Diagnostics in the Solar Transition Region and Corona, ed. J.-C. Vial & B. Kaldeich-Schümann (ESA SP-446; Noordwijk: ESA), 621
Sterling, A. C., & Moore, R. L. 2004, ApJ, 613, 1221
Straka, R. M., Papagiannis, M. D., & Kogut, J. A. 1975, Sol. Phys., 45, 131
Tanaka, K. 1991, Sol. Phys., 136, 133
Tandberg-Hanssen, E. 1974, Solar Prominences (Dordrecht: Reidel)
———. 1995, The Nature of Solar Prominences (Dordrecht: Kluwer)
Taylor, J. B. 1974, Phys. Rev. Lett., 33, 1139
Titov, V. S., & Démoulin, P. 1999, A&A, 351, 707
Tomczyk, S. 2004, AGU Abstr. Fall, 85, SH31B-04
Vaiana, G. S., Krieger, A. S., & Timothy, A. F. 1973, Sol. Phys., 32, 81
Vrsnak, B., Maricic, D., Stanger, A. L., & Veronig, A. 2004, Sol. Phys., 225, 355
Waldmeier, M. 1941, Ergebnisse und Probleme der Sonnenforschung (Lepizig: Becker & Erler)
———. 1970, Sol. Phys., 15, 167
Wolfson, R., Conover, C., & Illing, R. M. E. 1987, J. Geophys. Res., 92, 13641
Yurchyshyn, V. B. 2002, ApJ, 576, 493
Zirin, H. 1988, Astrophysics of the Sun (Cambridge: Cambridge Univ. Press)